Delft University of Technology

Elucidating the Impact of Functional Additives on the Structure and Ion Dynamics of Hybrid Solid Electrolytes

Zhang, Shengnan; Li, Yuhang; Bannenberg, Lars J.; Liu, Ming; Wagemaker, Marnix; Ganapathy, Swapna

DOI
10.1002/aenm.202406003

Publication date
2025

Document Version
Final published version

Published in
Advanced Energy Materials

Citation (APA)
Zhang, S., Li, Y., Bannenberg, L. J., Liu, M., Wagemaker, M., & Ganapathy, S. (2025). Elucidating the Impact of Functional Additives on the Structure and Ion Dynamics of Hybrid Solid Electrolytes. *Advanced Energy Materials*, *15*(26), Article 2406003. https://doi.org/10.1002/aenm.202406003

Important note
To cite this publication, please use the final published version (if applicable).
Please check the document version above.

Copyright
Other than for strictly personal use, it is not permitted to download, forward or distribute the text or part of it, without the consent of the author(s) and/or copyright holder(s), unless the work is under an open content license such as Creative Commons.

Takedown policy
Please contact us and provide details if you believe this document breaches copyrights.
We will remove access to the work immediately and investigate your claim.

This work is downloaded from Delft University of Technology.
For technical reasons the number of authors shown on this cover page is limited to a maximum of 10.

ADVANCED ENERGY MATERIALS
www.advenergymat.de

Elucidating the Impact of Functional Additives on the Structure and Ion Dynamics of Hybrid Solid Electrolytes

Shengnan Zhang, Yuhang Li, Lars J. Bannenberg, Ming Liu, Marnix Wagemaker,* and Swapna Ganapathy**

One of the major challenges in advancing polymer-inorganic hybrid solid electrolytes (HSEs) lies in comprehending and controlling their internal structure. In addition, the intricate interplay between multiple phases further complicates efforts to establish the structure-property relationships. In this study, by introducing a multifunctional LiI additive to an HSE compromising of polyethylene oxide (PEO) polymeric electrolyte and the fast lithium-ion conductor Li_6PS_5Cl, the relationship between the bulk and interface structure and ascertaining their impact on lithium-ion dynamics within the HSE is disentangled. Using multidimensional solid-state nuclear magnetic resonance, we find that the addition of LiI stabilizes the internal interfaces and enhances lithium-ion mobility. A kinetically stable solid-electrolyte interphase is formed at the lithium-metal anode, increasing the critical current density to 1.3 mA cm^{-2}, and enabling long-term stable cycling of lithium symmetric cells (>1200 h). This work sheds light on tailoring the structure of HSEs to improve their conductivity and stability for enabling all-solid-state lithium-metal batteries.

1. Introduction

Solid-state electrolytes (SSEs) are investigated for their superior safety, i.e., inflammable and leak-proof, compared to conventional liquid electrolytes. SSEs with high ionic conductivity, (electro)chemical stability, and easy processability are required to enable high-energy-density all-solid-state lithium (Li)-metal batteries (ASSLMBs), which appears to be one of the most appealing next-generation battery technologies.[1–4] However, the practical utilization of SSEs remains challenging due to the absence of a comprehensive single electrolyte possessing all the required properties. Among currently investigated SSEs, inorganic solid electrolytes (ISEs) typically suffer from severe sensitivity to ambient atmosphere, high resistance at the electrode/electrolyte interface, and instability in contact with Li, despite their remarkable ionic conductivity and mechanical strength.[5–7] Conversely, solid polymer electrolytes (SPEs) offer greater flexibility and favorable compatibility with Li, yet their room temperature conductivity tends to be relatively low ($<10^{-5}$ S cm^{-1}).[8,9] In this context, a hybrid concept that seeks to combine the advantages of both ISEs and SPEs, appears to be a promising solution for advancing the application of ASSLMBs.[10–12] In principle, the combination of ISEs and SPEs can result in a wide variety of combinations of different ion conductors and their respective ratios. One of the most extensively studied systems is the polyethylene oxide (PEO)-Li salt (LiX) matrix filled with ISEs fillers.

In the PEO-LiX matrix, Li-ion conduction occurs via the segmental motion of the polymer, which relies on the solvation of Li-ions through the lone electron pair donated from the oxygen atom of the PEO chain (via the bonding and fracturing of EO-Li bonds), allowing for the transport of Li-ions.[13,14] However, the molecular segmental motion is confined to the amorphous region, resulting in limited ionic conductivity. Embedding ISE fillers, thus forming hybrid solid electrolytes (HSEs), can reduce the degree of crystallinity of the polymer matrix and create additional fast Li-ion transport channels.[15–18] An ideal triple Li-ion conduction network is envisioned: i) within the PEO-LiX matrix; ii) along the organic/inorganic interface; and iii) through the ISE phase. However, achieving this ideal scenario remains challenging as the Li-ion conductivity of the obtained HSEs still falls short of the requirements for ASSLMBs. This is primarily due to the formation of an inert interface between the ISE fillers and the polymer, and the persistently high crystallinity of the polymer matrix. Various approaches have been proposed to address the

---

S. Zhang, L. J. Bannenberg, M. Wagemaker, S. Ganapathy
Section Storage of Electrochemical Energy
Radiation Science and Technology
Faculty of Applied Sciences
Delft University of Technology
Mekelweg 15, Delft 2629 JB, The Netherlands
E-mail: m.wagemaker@tudelft.nl; s.ganapathy@tudelft.nl
Y. Li, M. Liu
Shenzhen Key Laboratory of Power Battery Safety and Shenzhen Geim Graphene, Center
Tsinghua Shenzhen International Graduate School
Tsinghua University
Guangdong 518055, China
E-mail: liuming@sz.tsinghua.edu.cn

The ORCID identification number(s) for the author(s) of this article can be found under https://doi.org/10.1002/aenm.202406003

© 2025 The Author(s). Advanced Energy Materials published by Wiley-VCH GmbH. This is an open access article under the terms of the Creative Commons Attribution License, which permits use, distribution and reproduction in any medium, provided the original work is properly cited.

DOI: 10.1002/aenm.202406003

16146840, 0, Downloaded from https://advanced.onlinelibrary.wiley.com/doi/10.1002/aenm.202406003 by Technical University Delft, Wiley Online Library on [06/06/2025]. See the Terms and Conditions (https://onlinelibrary.wiley.com/terms-and-conditions) on Wiley Online Library for rules of use; OA articles are governed by the applicable Creative Commons License

aforementioned interlinked issues and reduce the crystallinity of the polymer phase. One common approach is the addition of plasticizers (e.g., tetraethylene glycol dimethyl ether, succinonitrile, ionic liquid), which mainly work on reducing the crystallinity of the polymer matrix.[19–23] However, this typically sacrifices the mechanical strength as well as the thermal and electrochemical stability of the HSEs. For instance, succinonitrile suffers from poor reduction stability and can undergo irreversible interfacial reactions with Li-metal anodes.[24,25] Alternatively, modifying the Li salt composition presents another strategy. The use of secondary salt additives can improve interfacial stability with electrodes, yet careful selection is required. Factors such as anion size, Li-ion coordination, and the solubility within the polymer matrix significantly impact phase compatibility. Poorly matched salts can lead to phase separation, disrupting ion transport pathways and diminishing overall performance.[26–28] Borate-based additives, such as lithium difluoro(oxalate)borate (LiBOB), enhance interfacial stability by forming stable passivating layers on electrodes. However, their bulky molecular structures can impede ionic conductivity, posing a trade-off between stability and ion transport.[29,30]

To address these issues, identifying additives for PEO-based HSEs that enable a conductive organic/inorganic interface, and reduce the crystallinity of the polymer matrix while maintaining certain mechanical strength presents a viable strategy. Simultaneously, it is necessary that the HSEs interact synergistically with Li-metal to form a mechanically and chemically stable solid-electrolyte interphase (SEI) layer with high conductivity. Recently, the incorporation of a binary LiI additive into sulfide solid electrolytes has been found to be advantageous, as LiI improves the Li-ion conductivity and Li-metal compatibility by suppressing the reductive decomposition of the sulfide solid electrolytes.[31–33] This suggests that the introduction of LiI in the PEO-LiX/sulfide-ISE can be highly advantageous. LiI is expected to lower the internal resistance by altering the interface structure of the PEO-LiX/sulfide-ISE.

Herein, through incorporating LiI (5 wt.%) in the PEO-LiTFSI-Li_6PS_5Cl hybrid system, we aim to unveil how this secondary Li salt phase modifies the interface structure between the organic/inorganic phases and how it changes the Li solvation structure in the PEO-LiX matrix. Targeted at activating the high conductivity of the inorganic Li_6PS_5Cl, multinuclear and multiscale solid-state nuclear magnetic resonance (NMR) are employed to address the major experimental challenge of disentangling the local Li-ion transport across the polymer phase, the inorganic phase, and the interface between these two phases. Building on previous research, a combination of 2D exchange (2D-EXSY),[34,35] pulsed field gradient (PFG), 1D direct excitation with/without decoupling, and cross-polarization (CP) dynamics NMR experiments are utilized.[34,36,37] A clearly improved self-diffusion process between the organic and inorganic phases is visualized and quantified by 2D ^6Li-^6Li EXSY, rationalizing the increased ionic conductivity observed with electrochemical impedance spectroscopy (EIS) measurements. Unraveling the bulk and local interfacial structures of the HSEs demonstrates that the addition of LiI facilitates Li dissociation in the bulk while impeding detrimental reactions between PEO and Li_6PS_5Cl. Through X-ray photoelectron spectroscopy (XPS) and time-of-flight secondary ion mass spectrometry (TOF-SIMS) analysis, a stable interface with Li-metal, rich in inorganic species, was identified that is instrumental in inhibiting the formation and aggregation of Li dendrites, thus facilitating stable and long cycling Li/HSE/Li symmetrical cells and enabling the use of sulfur cathodes.

2. Results and Discussion

2.1. Improving Li-ion Diffusion Between PEO-LiTFSI and Li_6PS_5Cl with a LiI Additive

To determine whether the inorganic phase actively contributes to the overall Li-ion conductivity, it is crucial to directly and non-invasively detect the Li-ion diffusion between the organic (PEO-LiTFSI) and inorganic (Li_6PS_5Cl, 10 wt.%) phases in the HSE system. 2D-EXSY experiments under magic angle spinning (MAS) conditions are employed to investigate the impact of LiI on the interfacial Li-ion conduction in the PEO-LiTFSI-Li_6PS_5Cl hybrid system. The exchange between distinct Li environments (in this case, LiTFSI-PEO and Li_6PS_5Cl, as depicted in **Figure 1a**) within the NMR time scale generates off-diagonal (cross) peaks in the 2D contour plots, marked by dotted boxes in Figure 1a–c. With the increase in mixing time (t_{mix}) or temperature, more Li-ions spontaneously diffuse between these environments, either due to longer mixing period or faster dynamics, leading to the emergence or growth of cross-peak intensity.

For $PEO_{18}LiTFSI$-Li_6PS_5Cl [EO:Li = 18:1 molar ratio, denoted as HSE (18:1)], no cross-peaks are visible in the 2D-EXSY spectrum (Figure S1a, Supporting Information) despite a relatively long t_{mix} at an elevated temperature (338 K). This is attributed to the accumulation of interfacial decomposition products on the Li_6PS_5Cl surface, which forms a barrier layer that impedes Li-ion diffusion and prevents this phase from contributing to the long-range conductivity of the HSE.[34] To address this limitation, LiI was introduced to the HSE system, with the initial goal of improving interfacial conductivity by modifying the composition and structure of the interface. When LiI is added to the HSE (18:1), forming $PEO_{18}LiTFSI$-Li_6PS_5Cl-LiI (denoted as HSE-LiI), cross-peaks are directly observed between the LiTFSI-PEO and Li_6PS_5Cl environments at room temperature (Figure 1a,b), even at a relatively short t_{mix} (Figure S1b, Supporting Information). In addition, an evident rise in cross-peak intensity is observed with increasing t_{mix} and temperature (Figure 1a,b; Figure S1b,c Supporting Information). Given the LiI peak (≈−4.56 ppm) is not observed in the one-pulse ^6Li NMR spectrum (Figure S2, Supporting Information), it is plausible that the LiI fully dissociates in the PEO matrix, consistent with previous reports.[40–42] As a result, the EO:Li ratio varies between these two samples, with the HSE-LiI sample effectively having an EO:Li ratio of 13:1. To have a more fair comparison, a sample with the same EO:Li ratio was prepared, i.e., $PEO_{13}LiTFSI$-Li_6PS_5Cl (EO:Li = 13:1 molar ratio, denoted as HSE (13:1)), serving as a more appropriate reference for examining the impact of LiI in the HSEs system. Hence from hereon, we compare the HSE-LiI with HSE (13:1), unless otherwise specified. It was found that increasing the salt concentration from 18:1 to 13:1 results in a noticeable reduction in the mechanical strength of the HSE membrane. As shown in Figure S3a–c (Supporting Information), the HSE-LiI membrane retains sufficient mechanical strength for handling.

© 2025 The Author(s). Advanced Energy Materials published by Wiley-VCH GmbH

16146840, 0, Downloaded from https://advanced.onlinelibrary.wiley.com/doi/10.1002/aenm.202406003 by Technical University Delft, Wiley Online Library on [06/06/2025]. See the Terms and Conditions (https://onlinelibrary.wiley.com/terms-and-conditions) on Wiley Online Library for rules of use; OA articles are governed by the applicable Creative Commons License

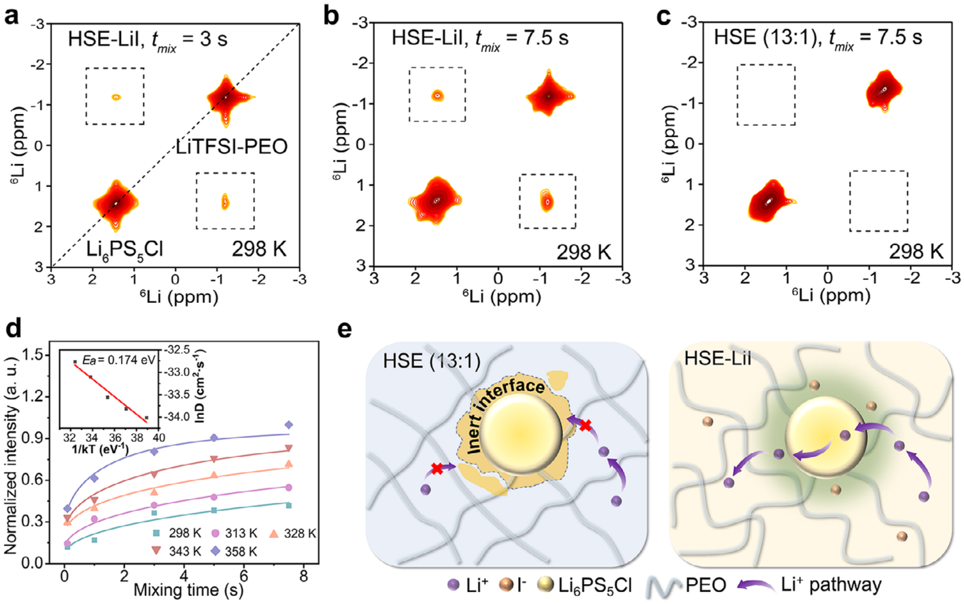

Figure 1. Measuring and quantifying Li-ion transport between the PEO-LiTFSI and Li_6PS_5Cl phases in the HSE system. 2D ^6Li-^6Li EXSY spectra measured with a) $t_{mix} = 3$ s, b) $t_{mix} = 7.5$ s for HSE-LiI, and c) $t_{mix} = 7.5$ s for HSE (13:1) at 298 K. d) Evolution of the normalized cross-peak intensity as a function of t_{mix} at the temperatures indicated in the graph. The inset figure illustrates the dependence of the diffusion coefficient (D), obtained by fitting the 2D ^6Li-^6Li EXSY data to a diffusion model described in detail elsewhere.[38,39] The normalized intensity is denoted in arbitrary units (a. u.). Fitting the temperature dependence of D to the Arrhenius law provides an activation energy (E_a) of 0.174 ± 0.02 eV. e) Schematic figure of Li-ion diffusion pathway in HSE (13:1) and HSE-LiI.

In contrast, the HSE (13:1) membrane is very sticky and challenging to process (Figure S3d,e, Supporting Information).

Fitting the normalized intensity of the cross-peak evolution to a diffusion model derived from Fick's law (Supplementary text 1), described in our previous work,[38,39] leads to diffusion coefficients as a function of temperatures (Figure 1d, inset). The local Li-ion diffusion between the organic and inorganic species in the HSE-LiI can thus be quantified. Fitting the diffusion coefficients with the Arrhenius law results in an activation energy (E_a) of 0.174 eV for this process, which is notably lower than that obtained from the EIS measurements (vide infra, 0.201 and 0.557 eV from Figure 4b). This disparity arises because the 2D-EXSY measurement probes local Li-ion diffusion across the organic/inorganic interfaces, whereas the EIS measurement primarily assesses bulk Li-ion conduction. This suggests that the incorporation of LiI alters the interface structure between the organic and inorganic components, transitioning it from an inert configuration to one that exhibits improved Li-ion conductivity, thereby enabling the participation of Li_6PS_5Cl particles in the overall Li-ion conduction (Figure 1e).

2.2. Impact of LiI on Bulk and Local Structures of the HSE

To understand how LiI interacts with the organic and inorganic phases in the HSE-LiI system and consequently improves the Li-ion mobility, it is essential to characterize both the bulk and local structures of the HSEs. The ^7Li NMR spectra in **Figure 2a** show that the Li-ion resonances are shifted downfield for the HSE-LiI electrolyte. The downfield shift of the LiTFSI-PEO peak is indicative of reduced electron density around the Li atoms, suggesting improved Li mobility within the PEO, which is a result of the enhanced dissociation degree of the LiTFSI.[41,43,44] The shift of the Li_6PS_5Cl peak likely stems from increased local disorder and partial intercalation of I^- anions into the structure, or exchange with Cl^-.[45] To isolate this effect from interactions with the LiTFSI-PEO environment, a control sample of Li_6PS_5Cl mixed with LiI in acetonitrile (Li_6PS_5Cl@LiI) was prepared. The Li_6PS_5Cl peak in this mixture also shows a downfield shift relative to pristine Li_6PS_5Cl (Figure S4, Supporting Information), demonstrating that LiI alone can alter the Li environment within the Li_6PS_5Cl phase. Notably, the ^1H peak also shifts to higher ppm for the HSE-LiI sample in the ^1H NMR spectrum (Figure S5, Supporting Information), signifying the interaction between the PEO chains and I^- anions.[40,41] Furthermore, Raman analysis was conducted to identify the $TFSI^-$ states (Figure 2b,c).[46] In HSE (13:1), the content of free $TFSI^-$, contact ion pairs (CIP), and aggregate clusters are 17.9%, 54.5%, and 27.7%, respectively, while the corresponding values for HSE-LiI are 33.1%, 37.7%, and 29.3%, respectively. The nearly doubled amount of free $TFSI^-$ suggests the presence of more "free" Li-ions due to the improvement in dissociation of the Li salt by the addition of LiI (Figure 2g), which is consistent with the peak shift shown in the ^7Li spectra (Figure 2a).

The bulk structure of the HSEs was further explored by XPS (Figures S6 and S7, Supporting Information). The signal at ≈292.8 and ≈288.2 eV in the C 1s spectra are attributable to the $-CF_3$ group of LiTFSI and the small amount of $-COOR$ from the PEO decomposition, such as Li_2CO_3 and $ROCO_2Li$.[47,48] The intensities of the peaks at ≈286.6 and ≈284.8 eV, corresponding to C—O—C and C—C/C—H of the PEO backbone, show a clear difference in ratio between HSE-LiI and HSE (13:1). This difference has not yet been addressed in publications, and presently it is

© 2025 The Author(s). Advanced Energy Materials published by Wiley-VCH GmbH

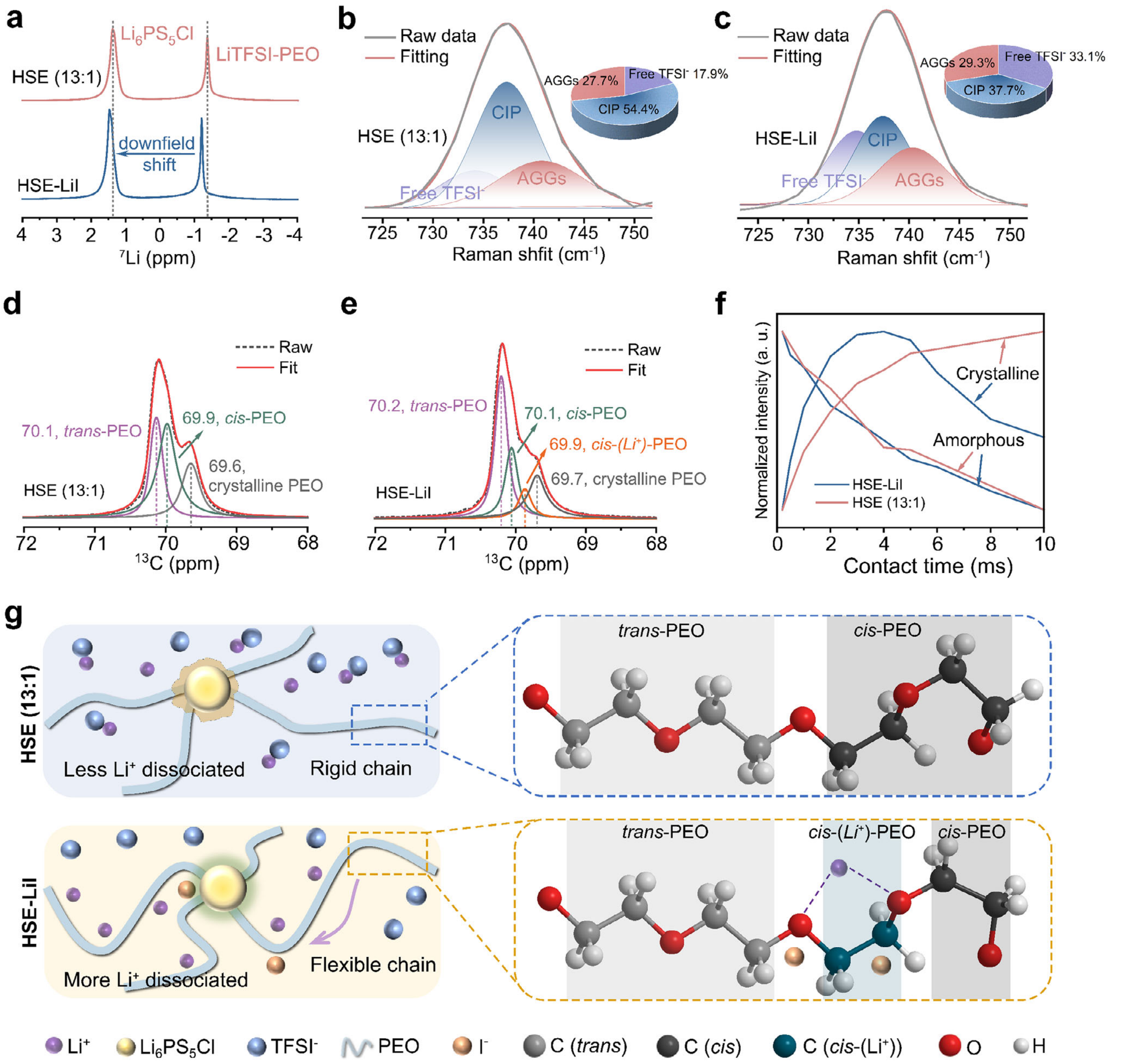

Figure 2. Characterizing the bulk structure of the HSEs with and without LiI. a) 1D ^{7}Li MAS spectra. Raman spectra of b) HSE (13:1), and c) HSE-LiI electrolytes and corresponding quantification results of the TFSI$^-$ anion states in the HSEs. CIP, contact ion pairs; AGGs, aggregate clusters. Fitting of the high power decoupling (hpdec) ^{13}C single-pulse spectra for d) HSE (13:1), and e) HSE-LiI. f) Integrated intensities extracted from the 1D ^{13}C CP MAS spectra obtained for HSE-LiI and HSE (13:1), expressed in arbitrary units (a. u.), with a focus on both the amorphous and crystalline ^{13}C environments as highlighted in Figure S10 (Supporting Information). g) Schematic showing the influence of LiI on the bulk structure of the HSE, with the carbon conformation of HSE-LiI and HSE (13:1) assigned in Figure 2d,e.

possibly attributed to the interaction between I$^-$ and C—C/C—H.[40] Two doublets centered ≈168.68 eV (S 2p$_{3/2}$) and ≈166.88 eV (S 2p$_{3/2}$) correspond to LiTFSI and its decomposition products, such as —SO$_2$CF$_2$$^+$ and Li$_x$S$_y$O$_z$.[47,49] A weak intensity doublet of polysulfides (-S$_x$^{0}-) is present in both samples, while additional P—S—Li bonds from Li$_6$PS$_5$Cl are observed in HSE (13:1).[50] The more intense PEO and LiTFSI peaks in the XPS spectra imply a relatively higher coverage of the organic phase on the surface of HSE-LiI. This corresponds to the scanning electron microscopy (SEM) images in Figure S8 (Supporting Information), where HSE-LiI displays a smoother surface and HSE (13:1) shows obvious agglomeration of Li$_6$PS$_5$Cl particles. Further characterization of the bulk structure of the HSEs was conducted using TOF-SIMS (Figure S9, Supporting Information). Secondary-ion fragments such as NS$_2$O$_4$C$_2$F$_6$$^-$, NSO$_2CF_3$$^-$, and C$_2H_3O^-$ are identified

© 2025 The Author(s). Advanced Energy Materials published by Wiley-VCH GmbH

16146840, 0, Downloaded from https://advanced.onlinelibrary.wiley.com/doi/10.1002/aenm.202406003 by Technical University Delft, Wiley Online Library on [06/06/2025]. See the Terms and Conditions (https://onlinelibrary.wiley.com/terms-and-conditions) on Wiley Online Library for rules of use; OA articles are governed by the applicable Creative Commons License

as representing the PEO-LiTFSI phase, while S^- and PS^- fragments originated from the Li_6PS_5Cl phase (with SO_2^- attributed to the oxidation of PS_x^- species).[51] 3D reconstruction and top-down depth profiles of the species of interest show stronger signals from the polymer matrix and weaker signals from the Li_6PS_5Cl phase in HSE-LiI, indicating a higher degree of organic coverage that further supports the aforementioned results.

A detailed study of the organic phase conformation is conducted using ^{13}C NMR. This is realized by high-power decoupling (hpdec) single-pulse ^{13}C experiments and 1D ^{13}C CP MAS ($^1H \rightarrow {}^{13}C$) (Figure 2d,e; Figure S10, Supporting Information). Deconvoluting the hpdec ^{13}C spectra reveals that the ^{13}C environments are dominated by *trans*-PEO, *cis*-PEO, and crystalline PEO in both the HSE-LiI and HSE (13:1) (Figure 2d,e; Table S1, Supporting Information).[52] An additional ^{13}C environment is present in the HSE-LiI spectrum, with a chemical shift close to that of the *cis*-PEO. This is attributed to the enhanced coordination between *cis*-PEO and Li-ion in the presence of I^-, which causes an upfield shift of the *cis*-PEO peak due to a more pronounced shielding effect [designated as *cis*-(Li^+)-PEO, see the carbon configuration in Figure 2g]. In contrast, the absence of this peak in HSE (13:1) indicates a weaker PEO-Li^+ coordination environment due to the absence of I^-. In analyzing the PEO matrix, it becomes crucial to discern the crystalline and amorphous phases, as the Li-ion transport within the PEO phase is governed by the segmental motion within the amorphous phase. This can be efficiently achieved using ^{13}C CP MAS NMR, as both the crystalline and amorphous phases exhibit distinct dependencies on the CP contact time (t_{CP}).[53] In these experiments, abundant protons (^1H) are utilized to identify ^{13}C environment in close vicinity (within a few atomic bond lengths) through magnetization transfer during the t_{CP} period. In the evolution of the ^{13}C CP MAS spectra, the peak intensity, varying with t_{CP}, notably relies on the local structure and the $^1H/^{13}C$ dynamics of the investigated system. The signal from the amorphous PEO phase is only detectable with a short t_{CP} after which the intensity decreases on increasing t_{CP} due to its high mobility, which reduces the efficiency of the dipolar interaction.[53,54] In contrast, the less mobile crystalline phase shows an increase in peak intensity with extended t_{CP}. Therefore, in Figure S10 (Supporting Information), the sharp peak is assigned to the crystalline phase, while the broad peak corresponds to the amorphous phase, as determined by their intensity evolution with t_{CP} and linewidth (Table S2, Supporting Information). Comparing the buildup of their peak intensity (Figure 2f), despite similar decay rates for the amorphous phase, the decay of the crystalline phase is accelerated by the presence of LiI, suggesting improved local ^1H dynamics of the HSE-LiI.

Based on the ^7Li, ^1H, ^{13}C hpdec, ^{13}C CP MAS NMR, and Raman results, a conformation diagram of the HSEs with and without LiI is proposed in Figure 2g. The impact of LiI on the bulk structure of the HSE encompasses several critical factors, notably promoting salt dissociation and reducing polymer crystallinity. The resulting increase in "free" Li-ions and enhanced polymer chain mobility collectively contribute to improved Li-ion diffusion. Furthermore, the assigned carbon configurations indicate the formation of a more Li-ion conductive polymer chain structure, highlighting a novel aspect of the HSE system that warrants further investigation.

The individual mobility of cations and anions was studied by PFG-NMR. The Li-ion diffusion in the PEO phase and the Li_6PS_5Cl phase can be readily distinguished as there is an appreciable difference between their ^7Li chemical shifts. The self-diffusion coefficients of ^7Li (D_{Li}) and ^{19}F (D_F) were measured at various temperatures (**Figure 3**a; Figure S11, Supporting Information). The D_{Li} in the PEO-LiTFSI phase is virtually identical in the HSEs regardless of the presence of LiI, but a higher D_{Li} is observed for the Li_6PS_5Cl phase in the HSE-LiI sample. This suggests that the increased conductivity resulting from the addition of LiI is associated with better participation of the Li_6PS_5Cl phase and/or better conductivity of the Li_6PS_5Cl phase itself. From the X-ray diffraction (XRD) patterns (Figure S12, Supporting Information), no obvious difference is observed between the Li_6PS_5Cl phase in these two samples. This suggests that the higher D_{Li} of the Li_6PS_5Cl phase in the HSE-LiI, as obtained from PFG-NMR, is unlikely due to any major structural changes in the Li_6PS_5Cl. Instead, it is more likely associated with changes in the surface properties of the Li_6PS_5Cl particles, i.e., the interface between PEO-LiTFSI and Li_6PS_5Cl phases, which could improve Li-ion transport between the two phases. In both samples, D_F is generally higher than D_{Li} in the PEO phase, as expected for the PEO-based polymer electrolyte, where Li-ions strongly coordinate with the EO groups.[55] The introduction of LiI does not significantly affect the dynamics of the $TFSI^-$ anion, as the D_F remains similar for both samples (Figure S11, Supporting Information).

The results from the PFG-NMR motivate an in-depth study on the impact of the added LiI on the interface between the organic and inorganic components. For this, 1D $^{6,7}Li$ CP MAS ($^1H \rightarrow {}^{6,7}Li$) and 2D ^1H-^6Li (^1H-^{13}C) heteronuclear correlation (HETCOR) experiments were performed (Figure 3b–e; Figures S13 and S14, Supporting Information). Similar to the 1D ^{13}C CP MAS experiments (Figure S10 (Supporting Information), the abundant ^1H works as a medium to detect $^{6,7}Li$ in close proximity through magnetization transfer during the contact time i.e., t_{CP}. Consequently, this aids in elucidating the interfacial ion dynamics and structure. In comparison to the ^6Li single-pulse excitation spectra (Figure S2, Supporting Information), additional resonances are resolved in the ^6Li CP MAS spectra from −0.7 to 1.2 ppm for both electrolytes (Figure 3b). These signals can be attributed to: i) impurities on the Li_6PS_5Cl surface given its inherently high reactivity, and ii) the reaction products between PEO-LiTFSI and Li_6PS_5Cl particles, delineated as interfacial products in Figure 3b.[49,51,56,57] Similar to the single-pulse spectrum, a downfield shift of the ^6Li signal is also observed in the ^6Li CP MAS spectrum of HSE-LiI. In addition, fewer interfacial products are detected in the HSE-LiI system. Examining the development of the ^6Li CP MAS signal with varying t_{CP} from 0.2 to 8 ms (Figure S13a,b, Supporting Information), a distinctly faster buildup of the LiTFSI-PEO peak is evident in the HSE (13:1) sample, suggesting lower mobility of Li-ions in the proximity of the PEO, or that the Li-ions are more tethered to the PEO segments (the more mobile it is, the harder it is to detect).[34]

To better resolve the ^6Li signals arising from the interfacial Li-containing species in the ^6Li CP MAS experiments, 2D ^1H-^6Li heteronuclear correlation (HETCOR) experiments were conducted with a short t_{CP} of 0.5 ms (Figure 3d,e). This enables

© 2025 The Author(s). Advanced Energy Materials published by Wiley-VCH GmbH

16146840, 0, Downloaded from https://advanced.onlinelibrary.wiley.com/doi/10.1002/aenm.202406003 by Technical University Delft, Wiley Online Library on [06/06/2025]. See the Terms and Conditions (https://onlinelibrary.wiley.com/terms-and-conditions) on Wiley Online Library for rules of use; OA articles are governed by the applicable Creative Commons License

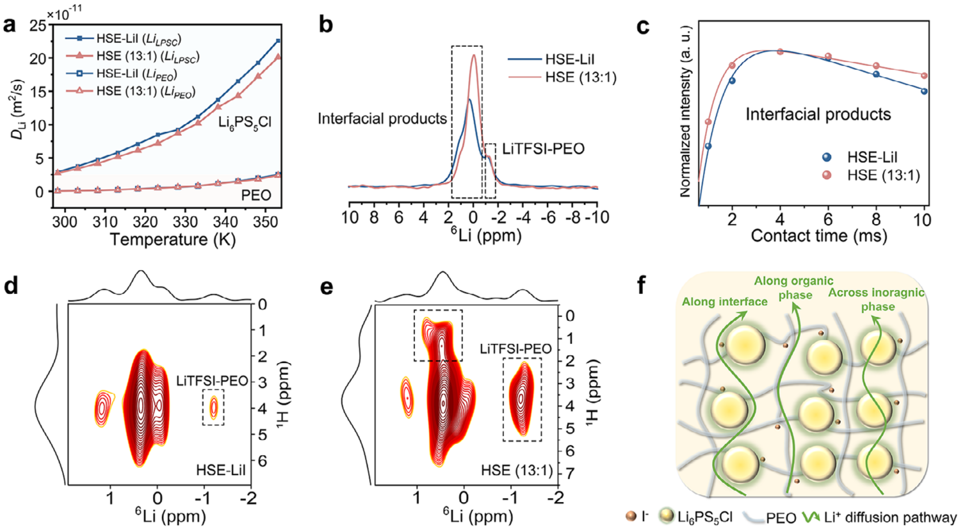

Figure 3. Identifying the interface structure of the HSEs with and without LiI. a) Self-diffusion coefficients of ^{7}Li (D_{Li}) obtained by PFG-NMR from 298 to 353 K, where the Li-ion diffusion in the PEO-LiTFSI phase (Li_{PEO}) and the Li_6PS_5Cl phase (Li_{LPSC}) are deconvoluted. b) 1D ^{6}Li CP MAS spectra with a t_{CP} of 8 ms (individual spectra with t_{CP} ranging from 0.2 to 8 ms are shown in Figure S13a,b, Supporting Information). c) Integrated intensities and the corresponding fits extracted from 1D ^{7}Li CP MAS spectra obtained for HSE-LiI and HSE (13:1), expressed in arbitrary units (a.u.), with a focus on the interfacial Li environment as highlighted in (b) (individual spectra with t_{CP} ranging from 0.05 to 10 ms are shown in Figure S15a,b (Supporting Information), see fitting details in Supporting Text 2). 2D ^{1}H-^{6}Li HETCOR spectra acquired with a t_{CP} of 0.5 ms of d) HSE-LiI, and e) HSE (13:1). f) Proposed Li-ion diffusion pathway in the HSE-LiI.

the detection of ^{6}Li directly bonded to ^{1}H or in its immediate proximity, and provides better-resolved ^{6}Li signals. Considerably stronger correlations between PEO and LiTFSI, as well as the interfacial products in the HSE (13:1), are observed, suggesting stronger coordination between Li-ions and EO units and lower mobility of the Li-containing species in close proximity to ^{1}H in this sample (Figure 3e). These findings are consistent with the ^{6}Li CP MAS spectra. The ^{6}Li signal in the HETCOR spectrum is dominated by the correlations between the ^{1}H in the main PEO chains ($-CH_2-CH_2-$) and ^{6}Li in its proximity. An additional ^{1}H environment is present in the HSE (13:1) sample (≈1 to 1.2 ppm, in the left dotted box in Figure 3e), and this ^{1}H resonance is correlated to the main ^{6}Li peak at ≈0.43 ppm as well. This is attributed to the degradation of PEO chains into shorter fragments due to side reactions with Li_6PS_5Cl.[51,58] Such degradation is also evident in the ^{1}H-^{13}C HETCOR spectra (Figure S14, Supporting Information), where additional ^{1}H-^{13}C correlations emerge in HSE (13:1) aside from the main correlation from the methylene groups in the PEO chains. The ^{1}H chemical shift also aligns with what is observed from the ^{1}H-^{6}Li HECTOR spectrum (Figure 3e). While the Li-containing interfacial products can be assumed to be similar regardless of the presence of LiI, the ^{1}H environments are different as evidenced by the additional ^{1}H environment detected for HSE (13:1) in the HETCOR spectra. Therefore, various ^{7}Li CP MAS experiments at different t_{CP} were performed to differentiate the ^{1}H dynamics (Figure S15, Supporting Information). Fits of the buildup of the interfacial products indicate a significantly faster cross-relaxation time for HSE-LiI compared to HSE (13:1) as shown in Figure 3c, which implies a more mobile interfacial Li environment in this sample. This disparity also leads to differences in proton $T_{1\rho}$ values ($T_{1\rho H}$, where $T_{1\rho}$ is the spin-lattice relaxation time in the rotating frame), as detailed in Table S3 (Supporting Information), with fitting details provided in Supplementary Text 2. The lower $T_{1\rho H}$ values for both the interface and the LiTFSI-PEO environments in HSE-LiI indicate faster proton dynamics in this sample.

In summary, the impact of LiI on the PEO-LiTFSI-Li_6PS_5Cl HSE system extends from the bulk to the interface. Dynamics derived from the PFG-NMR measurements reveal improved Li-ion diffusion in the Li_6PS_5Cl phase, suggesting improved interfacial Li-ion conduction between the PEO-LiTFSI and Li_6PS_5Cl phases. The 1D ^{6,7}Li CP MAS spectra indicate that the Li-ion transport over the organic/inorganic interface is facilitated by "cleaner" interfaces with faster local kinetics. Additionally, the 2D ^{1}H-^{6}Li and ^{1}H-^{13}C HETCOR spectra suggest that the structural stability is improved by suppressing side reactions between PEO and Li_6PS_5Cl. Combining the improved PEO chain mobility, mechanical stability, and Li salt dissociation in the bulk with stabilized organic/inorganic interfaces, Figure 3f presents a schematic illustration of Li-ion conduction in the LiI-modified HSEs. The Li-ion transport now occurs along the interface, through the organic phase, and across the inorganic phase.

2.3. Evaluation of Ionic Conductivity and Electrochemical Performance of the HSEs

Based on the aforementioned findings, it is evident that LiI positively activates the inert interface between the PEO-LiTFSI and Li_6PS_5Cl phases in the HSE. To complete the picture, electrochemical characterization of the HSE-LiI, HSE (13:1), and HSE (18:1) were performed. EIS results demonstrate that the addition of LiI in the HSE effectively improves the ionic conductivity compared to the HSEs with or without an increase in salt

© 2025 The Author(s). Advanced Energy Materials published by Wiley-VCH GmbH

16146840, 0, Downloaded from https://advanced.onlinelibrary.wiley.com/doi/10.1002/aenm.202406003 by Technical University Delft, Wiley Online Library on [06/06/2025]. See the Terms and Conditions (https://onlinelibrary.wiley.com/terms-and-conditions) on Wiley Online Library for rules of use; OA articles are governed by the applicable Creative Commons License

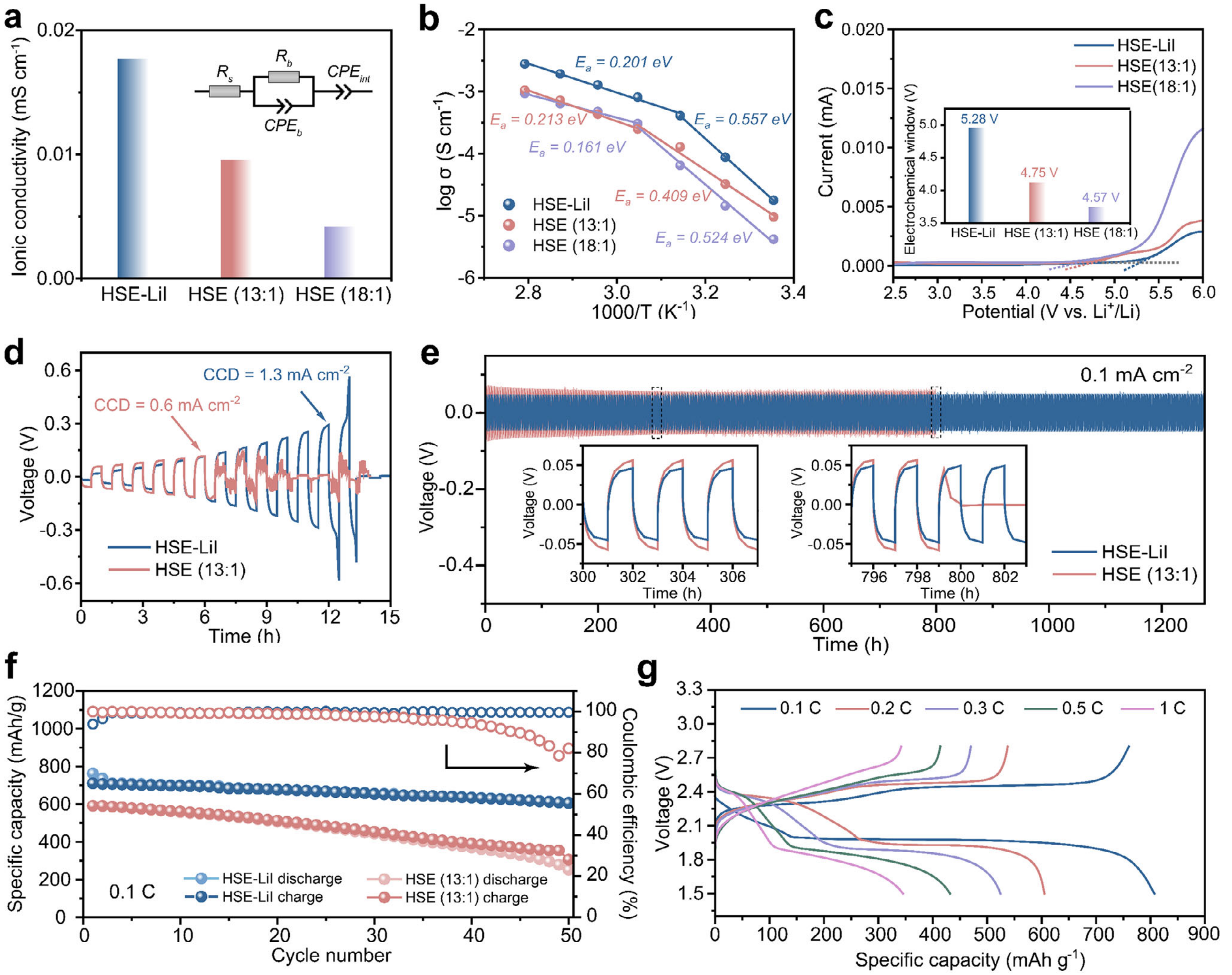

Figure 4. Macroscopic Li-ion diffusion and electrochemical characterizations of the HSEs. a) Ionic conductivity obtained from the fits in Figure S16 (Supporting Information) for the cells using different HSEs. The measurements were conducted using EIS at 25 °C. b) Arrhenius plots of the HSEs with fitted activation energies corresponding to different processes. c) LSV measurements of the Li/HSE/SS (SS: stainless steel) cells using different HSEs. d) CCD measurements for the HSE-LiI and HSE (13:1) with a stripping/plating period of 30 min. e) Galvanostatic voltage profiles of the Li/HSE/Li symmetric cells measured at 0.1 mA cm^{-2} and 40 °C (0.1 mAh cm^{-2}, with inserts showing the voltage profiles at ≈303 and ≈800 h). f) Cycling performance and Coulombic efficiency (CE) of the all-solid-state Li//S@CNTs cells using HSE-LiI or HSE (13:1) electrolyte at 0.1 C and 60 °C. The empty circles at the top correspond to CE (blue: Li/HSE-LiI/S@CNTs cell; orange: Li/HSE (13:1)/S@CNTs cell). g) Galvanostatic charge-discharge profiles of the all-solid-state Li/HSE-LiI/S@CNTs cells at various C-rates and 60 °C.

concentration (**Figure** 4a). The ionic conductivity of HSE (13:1) shows improvement only in the low-temperature range compared to HSE (18:1), which can be expected as the Li-ion transport is governed by the segmental motions of the PEO chains in these two samples. Increasing the salt concentration to a certain extent can reduce the crystallinity of the PEO phase.[59,60] However, at higher temperatures, almost all the PEO chains become mobile, resulting in no discernible differences in the Li-ion conducting ability in the polymer phase. In both HSEs, temperature-dependent conductivities reveal two processes with distinct slopes (Figure 4a). In the HSE-LiI, the critical temperature for these processes is lower than that in the other two HSEs, indicating a more amorphous structure in this sample. This is also reflected in the Li-ion transference number (t_{Li+}) measurements, where the HSE-LiI (t_{Li+} = 0.36) shows more than double the t_{Li+} compared to the HSE (13:1) (t_{Li+} = 0.17) (Figure S17, Supporting Information). This trend is consistent with the differential scanning calorimetry (DSC) results, which show that the HSE-LiI exhibits lower glass transition temperature (T_g) and melting temperature (T_m), as well as reduced crystallinity (Figure S18 and Table S4, Supporting Information).[49] Also, in the FT-IR spectra, the peaks corresponding to CH_2 stretching (υ) and wagging (ω) vibrations show a decrease in intensity for the HSE-LiI (Figure S19, Supporting Information), indicating the crystallinity of the polymer matrix reduces due to the interactions between HSE and LiI.[40,61,62] In addition, the peak ≈1620 cm^{-1} indicates the formation of C = C peak for the HSE without LiI additive. This is indicative of the degradation of PEO, via

© 2025 The Author(s). Advanced Energy Materials published by Wiley-VCH GmbH

16146840, 0, Downloaded from https://advanced.onlinelibrary.wiley.com/doi/10.1002/aenm.202406003 by Technical University Delft, Wiley Online Library on [06/06/2025]. See the Terms and Conditions (https://onlinelibrary.wiley.com/terms-and-conditions) on Wiley Online Library for rules of use; OA articles are governed by the applicable Creative Commons License

deprotonation through a series of fragment reactions.[56,63] The E_a of HSE-LiI is not notably lower than that of the HSEs without LiI (Figure 4b). This is attributed to the activated interfacial Li-ion conduction introduced by adding LiI to the HSE system, which involves three processes in calculating the energy barrier: Li-ion diffusion in the PEO-LiTFSI phase, at the interfaces, and within the Li_6PS_5Cl phase. In contrast, the other two samples lack the latter two diffusion pathways. The electrochemical stability window of the HSEs was determined by linear-sweep voltammetry (LSV) measurements (Figure 4c), where the HSE-LiI exhibits the highest stability window up to 5.28 V, and the HSEs without LiI show much narrower stability window of 4.75 V [HSEs (13:1)] and 4.57 V [HSE (18:1)], respectively. The narrow window in the PEO-LiTFSI-Li_6PS_5Cl HSE is attributed to the unstable interfaces between PEO-LiTFSI and Li_6PS_5Cl, which intensify the decomposition of the Li_6PS_5Cl particles and the degradation of the PEO chains, consequently resulting in incomplete Li-ion transport channels.[34,51,56] The widened window of the HSE-LiI thus also indicates that the addition of LiI is beneficial for suppressing the side reactions between the PEO-LiTFSI and the Li_6PS_5Cl particles.

The impact of LiI on the interfacial stability between the HSEs and Li-metal anodes is conducted in Li//Li symmetrical cells. During long-term cycling at 0.1 mA cm^{-2} and 40 °C (Figure 4e), the cell cycle with HSE (13:1) consistently shows a higher overpotential than HSE-LiI, especially at the beginning of the cycling (from ≈87 to ≈58 mV), which is ascribed to insufficient Li-ion conductivity and severe side reactions. In contrast, the cell using HSE-LiI maintained a stable overpotential at ≈48 mV and remained stable for over 1200 h, while the cell with HSE (13:1) failed at ≈800 h (Figure 4e). In addition, the Li/HSE-LiI/Li cell presents a critical current density (CCD) of 1.3 mA cm^{-2}, which is much higher than that for HSE (13:1) (0.6 mA cm^{-2}) (Figure 4d). Furthermore, temperature-dependent EIS measurements (Figure S20, Supporting Information) reveal that the Li/HSE-LiI/Li cell shows lower resistances and E_a compared to the HSE (13:1) counterpart, indicating faster charge transfer kinetics in the Li/HSE-LiI/Li cell. These results suggest that the interfacial stability toward Li-metal and the ability to suppress Li dendrites can be effectively improved by the presence of LiI. To further assess the interfacial compatibility of the HSE-LiI with the cathode, ASSLMBs were assembled with a cathode composite of sulfur with carbon nanotubes (S@CNTs) and a Li-metal anode using the HSE-LiI or HSE (13:1) as electrolyte. The high theoretical capacity (1675 mAh g^{-1}) and abundance of sulfur make it a promising cathode material.[64] In addition, LiI is known to stabilize the SEI and suppress the polysulfide shuttle in Li-S batteries,[65–67] while also enhancing interfacial stability and suppressing dendrite formation in sulfide solid electrolytes.[32,33,68,69] The Li/HSE-LiI/S@CNTs cell delivers a discharge capacity of ≈610 mAh g^{-1} after 50 cycles at 0.1 C and 60 °C, with an average Coulombic efficiency of ≈99.6% after the first two cycles (Figure 4f). The rate capability, depicted in Figure 4g, reveals discharge capacities of 807, 605, 523, 429, and 345 mAh g^{-1} at 0.1, 0.2, 0.3, 0.5, and 1 C, respectively. The dQ/dV profile of the first cycle at 0.1 C reveals multi-step redox reactions characteristic of the S cathode, similar to those observed in liquid electrolyte systems (Figure S21, Supporting Information).[70,71] This suggests efficient Li-ion transport and good electrolyte/electrode interfacial compatibility enabled by the HSE-LiI electrolytes. In contrast, the cell using HSE (13:1) as electrolyte exhibits a lower discharge capacity of ≈306 mAh g^{-1} under the same conditions (Figure 4f), with a much more rapid capacity decline during the rate test (Figure S22, Supporting Information).

2.4. Interfacial Stability of HSE-LiI with Li-Metal

To understand the origin of the improved interfacial stability of the HSEs toward Li-metal, both the pristine HSEs and the SEI formed on the Li-anode disk after cycling (20 cycles at 0.1 mA cm^{-2}) were investigated by depth-profiling XPS in conjunction with TOF-SIMS. **Figure** 5a–d shows the depth-dependent evolution of the C 1s and F 1s XPS spectra for the HSE-LiI and HSE (13:1). In the C 1s spectra, similar to the pristine HSEs shown in Figure S6 (Supporting Information), the C—C/C—H peak is from the ether groups of the PEO residues, while small peaks C—O and C = O originate from the decomposition products of PEO.[47,48] The PEO residues and the decomposition products of PEO form the amorphous outer layer of the SEI and continue deeper into the HSE (13:1) sample. It is worth noting that for the HSE (13:1), part of the decomposed species (C═O) are distributed in the inner layer of the SEI, implying the formation of a more organic-rich SEI.

In the F 1s spectra (Figure 5c,d), two peaks centered at ≈684.5 eV (LiF from the decomposition of LiTFSI) and ≈688.08 eV (—CF_3 group from the residual LiTFSI) were observed for both samples.[51,72] Apparently, a more LiF-rich SEI was formed on the Li disk cycled with HSE-LiI, with LiF distributed across both the outer and inner layers. Furthermore, upon tracking the relative spectral contribution of the O 1s species with etching (Figure S23, Supporting Information), a dominant distribution of the Li_2O component inside, accompanied by a small amount of organic $ROCO_2Li$ and C—O—C species on the surface, was observed in the SEI formed with HSE-LiI.[47,73] In the S 2p spectra (Figure S24a,b, Supporting Information), the doublet at ≈160 eV is attributed to the S^{2-} ions within Li_6PS_5Cl.[51,74] Besides, smaller doublets of -SO_2CF_3 (at ≈168.8 eV, S $2p_{3/2}$) and -$SO_2CF_2^+$/$Li_xS_yO_z$ (at ≈167.5 eV, S $2p_{3/2}$), associated with LiTFSI decomposition, were observed.[47,49] Apparently, there is more "free" S^{2-} and decomposed residual Li salt remaining on the surface of the SEI formed with HSE (13:1). A weaker LiTFSI signal (at ≈398.6 eV) was detected in the SEI formed with HSE (13:1), as indicated by the N 1s spectra (Figure S24c,d, Supporting Information).[40] This is in agreement with the rougher surface morphology of the HSE (13:1) electrolyte, as depicted in Figure S8 (Supporting Information), suggesting a lower amount of polymer phase distributed over the surface. A doublet at ≈618.6 and ≈630.1 eV were observed in the I 3d spectra, confirming the formation of the LiI compound in the Li/HSE-LiI interface (Figure S25, Supporting Information).[41,75]

TOF-SIMS top-down depth profiles and their corresponding 3D reconstruction for the species of interest were conducted to further detail the SEI composition and microstructure (Figure 5e,f). It is evident that CH mainly disperses on the top of the SEI, while a large amount of LiF is concentrated in the interior part, with some iodine ions (I^-) being homogeneously distributed within the SEI formed after cycling with HSE-LiI

© 2025 The Author(s). Advanced Energy Materials published by Wiley-VCH GmbH

16146840, 0, Downloaded from https://advanced.onlinelibrary.wiley.com/doi/10.1002/aenm.202406003 by Technical University Delft, Wiley Online Library on [06/06/2025]. See the Terms and Conditions (https://onlinelibrary.wiley.com/terms-and-conditions) on Wiley Online Library for rules of use; OA articles are governed by the applicable Creative Commons License

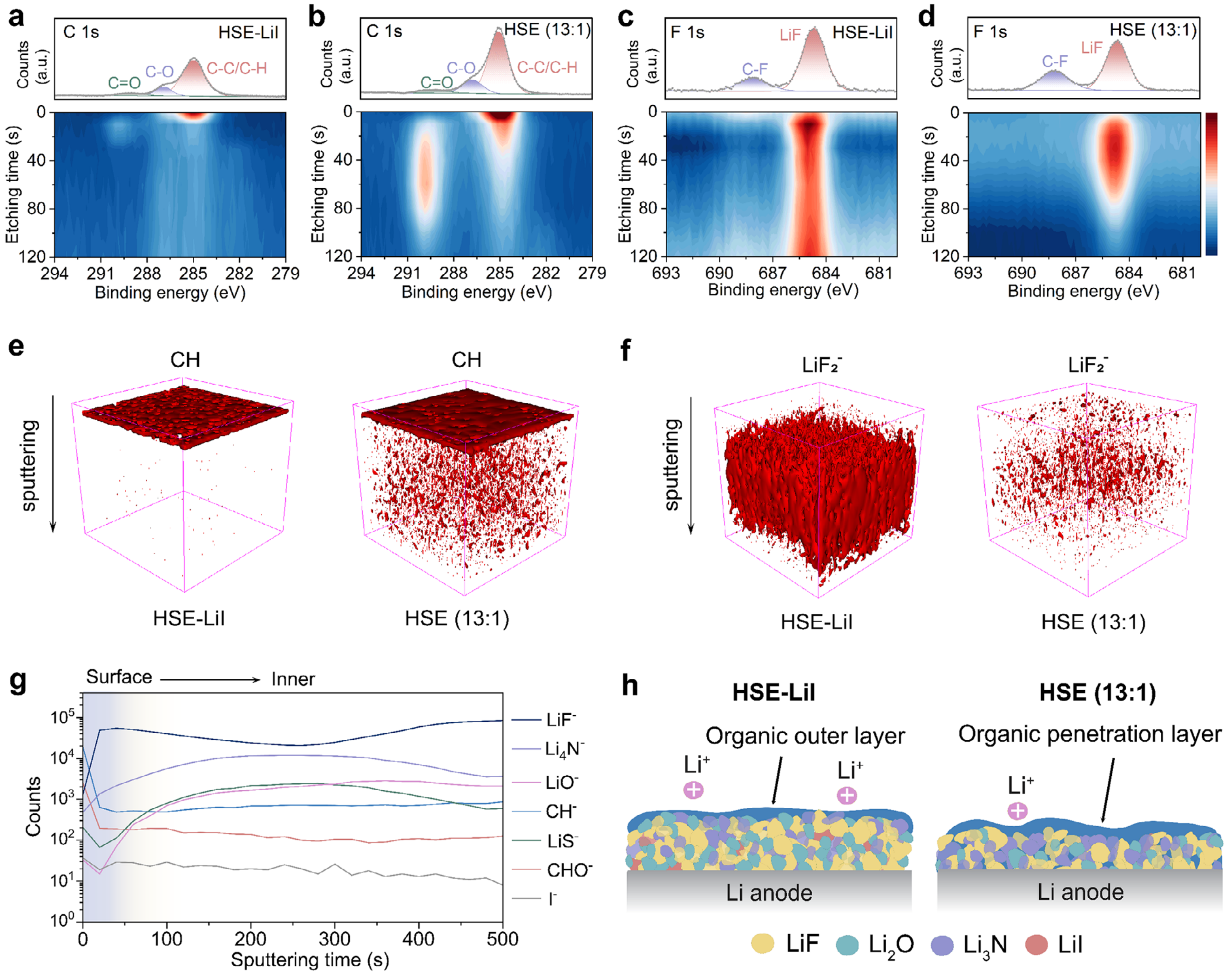

Figure 5. Assessing the interfacial properties of the HSEs with Li-metal anode. Depth-profiling XPS measurements of C 1s and F 1s for the Li-metal anode cycled with a,c) HSE-LiI, b,d) HSE (13:1). Each plot comprises two individual figures, i.e., the point before etching (up) and depth profiling spectrum (down). The color bar indicates the intensity from weak to strong from bottom to top. 3D reconstruction of TOF-SIMS secondary-ion fragments sputtered from the Li-metal anode cycled with HSE-LiI and HSE (13:1) electrolytes, respectively. The sputtered area is 100 × 100 μm^2. The species containing e) CH and f) LiF_2^- signals were selected, which are the main compounds of the investigated SEI layer. g) TOF-SIMS depth profiles of representative components of the SEI formed at the Li/HSE-LiI interface. h) Schematic showing the main components in the SEI formed at the Li/HSE-LiI and the Li/HSE (13:1) interfaces, respectively. For HSE-LiI, the SEI has an organic outer layer and a compact, inorganic-rich inner layer that is more Li-ion conductive, while for HSE (13:1), the SEI is more organic and less conductive. For both the depth-profiling XPS and TOF-SIMS measurements, the Li-metal electrodes were obtained by disassembling the Li/HSE/Li symmetrical cells cycled with HSE-LiI or HSE (13:1) electrolytes at 0.1 mA cm^{-1} for 20 cycles (0.1 mAh cm^{-1}, 40 °C).

(Figure S26, Supporting Information). In contrast, for the SEI obtained by cycling with HSE (13:1), more concentrated CH with less LiF is distributed in the inner layer. The depth profiles of the main chemical compounds of the investigated SEI cycled with HSE-LiI are depicted in Figure 5g. As the sputtering time increases, the evolution of these fragments initially exhibits a signal attenuation but stabilizes as the sputtering progresses. Inorganic species such as LiF, Li_3N, and Li_2O dominate in the SEI, which is in stark contrast with the SEI formed in Li/HSE (13:1) (Figure S27, Supporting Information). These observations are consistent with the XPS results, where a more inorganic-rich SEI was also detected for HSE-LiI. A schematic interpretation is provided in Figure 5h, which illustrates the SEI structures formed for the HSE-LiI and HSE (13:1), respectively, as determined by depth-profiling XPS and TOF-SIMS. For HSE-LiI, the SEI features an organic outer layer and a more compact, inorganic-rich inner layer that enhances Li-ion conductivity. In contrast, the SEI formed with HSE (13:1) is more permeated by the organic phase, resulting in a structure that is less conductive for Li-ions. This inorganic-rich SEI layer is considered pivotal in improving the interfacial stability of the Li/HSEs, which plays a prominent role in inhibiting dendrite propagation and promoting Li-ion conduction across the Li/SEI/HSE interfaces. Furthermore, the improved Li-ion conductivity, optimized solvation

© 2025 The Author(s). Advanced Energy Materials published by Wiley-VCH GmbH

16146840, 0, Downloaded from https://advanced.onlinelibrary.wiley.com/doi/10.1002/aenm.202406003 by Technical University Delft, Wiley Online Library on [06/06/2025]. See the Terms and Conditions (https://onlinelibrary.wiley.com/terms-and-conditions) on Wiley Online Library for rules of use; OA articles are governed by the applicable Creative Commons License

structure, and sufficient mechanical strength of the HSE-LiI work synergistically to promote uniform Li deposition and more effectively distribute local stress.

2.5. Impact of Local and Bulk Structures in HSEs

Understanding and controlling the internal structure of HSEs and their interface with the Li-metal anode is crucial for optimizing the structure-property relationships that dictate the performance of Li-metal batteries. Here, we introduce LiI to improve both the bulk and interfacial structures in the PEO-LiTFSI-Li_6PS_5Cl hybrid system and study in detail the structure-property relationship. The influence of LiI on the HSE manifests in two aspects: Li-ion diffusivity and the stability of the Li/HSE interface. The improvement of Li-ion diffusion on adding LiI is seen via the higher ionic conductivity and t_{Li+} obtained from the EIS measurements on the macroscopic scale (Figure 4a,b; Figure S20, Supporting Information). This result is supported by the intensified equilibrium Li-ion exchange between the organic phase (PEO-LiTFSI) and the inorganic phase (Li_6PS_5Cl), a phenomenon visualized and quantified by 2D ^{6}Li-^{6}Li EXSY NMR (Figure 1). It is worth noting that the E_a derived from the 2D-EXSY experiments (0.174 eV, Figure 1d) is lower than that obtained from the EIS measurements (0.201 and 0.557 eV, Figure 4b). This discrepancy indicates that both the interface and polymer phase properties notably influence Li-ion transport in the HSEs. Furthermore, the ^{1}H dynamics have been differentiated by ^{7}Li CP MAS experiments with various t_{CP}, from which the faster cross-relaxation time for HSE-LiI compared to HSE (13:1) suggests a more mobile interfacial Li environment between PEO-LiTFSI and Li_6PS_5Cl in the presence of LiI (Figure 3c; Figure S15, Supporting Information). This is further supported by the improved local ^{1}H dynamics in the HSE-LiI sample, as evidenced through ^{13}C CP MAS measurements at varying t_{CP} (Figure 2f). Nonetheless, the individual ^{7}Li mobility detected by PFG-NMR indicates that the Li-ion self-diffusion over the polymer matrix remains similar, regardless of the presence of LiI, though appears to differ for the inorganic phase or at the inorganic/organic interfaces (Figure 3a). Another pertinent aspect is the stabilized Li/HSE-LiI interface. This is seen via the widened stability window (5.28 V), higher CCD (1.3 mA cm^{-2}), and more stable long-term cycling in the Li/HSE/Li symmetric cells. This renders the HSE applicable to the all-solid-state Li-S battery system (Figure 4c–g).

Combining the above results, it becomes clear that the addition of LiI facilitates both the Li salt dissociation in the bulk HSE and interfacial Li-ion diffusion across the organic/inorganic interfaces. This illustrates that the effect of LiI extends from the bulk to the inner interfaces, impacting both structure and ion-dynamics. Additionally, the interactions between the HSE and LiI also improve its stability toward the Li-metal anode. XPS and TOF-SIMS suggest more PEO phase coverage on the surface of HSE-LiI, also seen from its smoother surface morphology in SEM (Figures S6–S9, Supporting Information). This explains the more stable Li/HSE-LiI interface, as typically a PEO-based SPE is more compatible with the Li-metal anode than Li_6PS_5Cl.[11] The single-pulse ^{6,7}Li NMR spectra indicate that LiI has fully dissociated in the HSE. The change in the chemical shift of the ^{7}Li peak suggests that the occurrence of more mobile Li-ions, as evidenced in the Raman spectra, leads to an increase in the amount of Li-ions coordinated to the PEO chains.[41,43,44] (Figure 2a–c) Besides, the downfield shift of the ^{1}H peaks and the appearance of the additional ^{13}C peak indicate an interaction between the I^- anions and the PEO chains.[40,41] (Figure S5; Figure 2e) The local interfacial structure, as detected by ^{6}Li CP MAS and ^{1}H-^{6}Li HETCOR experiments, suggests suppressed side reactions between PEO and Li_6PS_5Cl phases due to the addition of LiI, which has been further supported by 2D ^{1}H-^{13}C HETCOR spectra (Figure 3b–e; Figure S14, Supporting Information). Discriminating between the local amorphous and crystalline phases based on their respective t_{CP} dependence in the ^{13}C CP MAS experiments, higher local ^{1}H dynamics are observed in HSE-LiI based on the accelerated decay of its crystalline phase (Figure 2f), implying improved chain mobility.

The depth-profiling XPS and TOF-SIMS data suggest that the addition of LiI changes the decomposition subsequence of LiTFSI, tuning the growth dynamics of the SEI and leading to the formation of a more inorganic-rich SEI layer abundant in LiF, Li_2O, and Li_3N, coupled with an organic outer layer (Figure 5h). This SEI structure, rich in inorganic species, is well-known to be beneficial for effective Li-ion transport and uniform Li-metal deposition. LiF is electronically insulating and can prevent excessive electrolyte oxidation, while Li_2O promotes the formation of an anion-derived SEI by facilitating electron transfer.[76–79] Additionally, thermodynamically favored Li-Li_3N interactions guide uniform Li deposition.[80,81]

It is thus evident that the local and bulk structures jointly determine the properties of the HSEs. An effective percolation network of ionic conduction within the HSEs requires active interfacial Li-ion diffusion as well as a favorable bulk structure. The structure-property relationship of HSEs, investigated by incorporating LiI into the PEO-LiTFSI-Li_6PS_5Cl hybrid system, introduces a viable approach. While previous studies have incorporated LiI into either the polymer or sulfide phases, this work is the first to explore its effects within a hybrid system. The functional LiI additive simultaneously improves Li-ion transport while preserving the mechanical integrity of the HSE, as well as stabilizing both the organic/inorganic interfaces within the HSE and the electrolyte/Li-metal interface. This stands in clear contrast to widely studied plasticizer-type additives and Li salt modifications, which often entail a compromise between ionic conductivity, mechanical strength, and interfacial stability.[29] This novel combination suggests that fine-tuning the bulk properties synergistically stabilizes the interfaces within the polymer-Li salt-filler system, an aspect that was previously poorly understood. The influence of the LiI additive is also reflected in the improved stability of the Li/HSEs interface, further highlighting the importance of regulating and stabilizing interfaces to enable ASSLMBs. Reflecting on the structure-property-performance relationship, the present work provides insights into the rational regulation of various aspects of the HSE structure, from bulk to interface, with potential applicability to other electrolyte systems.

3. Conclusion

In summary, this work investigates the structure-property relationship of HSEs through the introduction of a LiI additive into

© 2025 The Author(s). Advanced Energy Materials published by Wiley-VCH GmbH

16146840, 0, Downloaded from https://advanced.onlinelibrary.wiley.com/doi/10.1002/aenm.202406003 by Technical University Delft, Wiley Online Library on [06/06/2025]. See the Terms and Conditions (https://onlinelibrary.wiley.com/terms-and-conditions) on Wiley Online Library for rules of use; OA articles are governed by the applicable Creative Commons License

the PEO-LiTFSI-Li_6PS_5Cl HSE system. The interaction between the HSE and LiI enhances Li-salt dissociation and reduces the crystallinity of the bulk PEO matrix while also stabilizing the organic/inorganic interfaces, thus improving the overall ionic conductivity. The bulk and interface structures revealed by multi-dimensional NMR experiments suggest that the addition of LiI mitigates the degradation of the PEO phase and its reactions with Li_6PS_5Cl, leading to a more Li-ion conductive interface environment and thereby improving the interfacial Li-ion diffusion. Besides, given the altered decomposition sequence of LiTFSI, a more inorganic-rich (i.e., LiF, Li_2O, and Li_3N) SEI was formed at the Li/HSE-LiI interface, which facilitates the Li-ion transport and suppresses dendrite propagation. The introduction of the multifunctional LiI additive provides perspective on the rational design of the internal structure of the HSE system, as well as the Li/HSE/cathode interfaces, providing insights for the practical application of high-safety and high-energy-density ASSLMBs.

4. Experimental Section

Preparation of Hybrid Solid Electrolytes: For the HSE-LiI and HSE (18:1) membranes, 384 mg PEO powder (M_w = 600, 000 g mol^{-1}, Sigma-Aldrich), 140 mg LiTFSI (Sigma-Aldrich), and 52.4 mg Li_6PS_5Cl (10 wt.%, NEI Corporation) were first homogeneously mixed with and without 26.2 mg LiI (5 wt.%, Sigma-Aldrich) in a mortar by grinding, then added into 7 mL acetonitrile (Sigma-Aldrich) and stirring for 24 h. The mixer used is an IKA Magnetic Stirrers RCT basic, operated at a stirring speed of 400–550 rpm at room temperature. The obtained homogenized slurry was cast onto a Teflon plate and dried in the glove box at room temperature for 24 h, and further dried under vacuum for 48 h. The HSE (13:1) membranes were prepared using the same procedures with 347 mg of PEO powder, 177 mg of LiTFSI, and 52.4 mg of Li_6PS_5Cl. The Li_6PS_5Cl@LiI mixture was prepared by mixing 52.4 mg Li_6PS_5Cl and 26.2 mg LiI in 10 mL acetonitrile at room temperature for 24 h, then dried in the glove box for 24 h, and further dried under vacuum for 48 h.

Material Characterizations: Raman spectra were acquired using a miniature laser confocal Raman spectrometer (Renishaw inVia Qontor) with a 785 nm laser at room temperature. For scanning electron microscope (SEM) imaging, the samples were transferred into an SEM (JEOL JSM-6010LA) machine under dry argon conditions by an air-tight Ar-filled sample holder. The images were taken using an accelerating voltage of 10 kV (secondary electron). Bragg-Brentano X-ray diffraction (XRD) measurements were conducted on an X'Pert Pro X-ray diffractometer (PANalytical) with Cu Kα radiation (λ_1 = 1.540598 Å and λ_2 = 1.544426 Å, at 45 kV and 40 mA) using an in-house air-tight holder. Differential scanning calorimetry (DSC) measurements were carried out at 10° min^{-1} step using a commercial TA-Q2000 DSC calorimeter (TA instruments). Fourier transform infrared spectroscopy (FT-IR) spectra were collected on Bruker VERTEX 70 spectrometer in an attenuated total reflection (ATR) mode. X-ray photoelectron spectroscopy (XPS) measurements were performed with a Thermo Fisher K-Alpha spectrometer to investigate the chemical compositions of both the pristine HSEs and the cycled Li electrodes. The samples were transferred into the XPS machine under vacuum using an air-tight sample holder. The spectrometer is equipped with a focused monochromatic Al kα source (1486.6 eV) anode operating at 36 W (12 kV, 3 mA), a flood gun operating at 1 V, 100 µA. The base pressure of the analysis chamber was ≈2 × 10^{-9} mbar and the spot size was ≈800 × 400 um^2. For the detailed scan collected before etching, a pass energy of 50 eV was used. Depth profiling was performed with an Ar^+ ion gun operated at 3 kV, corresponding to ≈0.5 nm s^{-1} as calibrated on Ta_2O_5, and a pass energy of 200 eV was used. In the analysis, the binding energy was corrected for the charge shift relative to the primary C 1s hydrocarbon peak at $BE = 284.8$ eV. For each sample, at least three points were measured which showed similar results. The data were fitted using 70% Gaussian and 30% Lorentzian line shapes (weighted least-squares fitting method) and nonlinear Shirley-type background using the Thermo Fisher Avantage software. Time-of-flight secondary ion mass spectrometry (TOF-SIMS) measurements were carried out on a Nano TOF-2 instrument (ULVAC-PHI, Japan) equipped with a Bi^{3++} beam (30 kV, 2 nA) cluster primary-ion gun for analysis, and an Ar^+ beam (3 keV, 100 nA) using a sputtering rate of 0.1 nm s^{-1} to obtain the desired depth profile. The area of analysis was 100 × 100 µm^2, whereas the sputtering area was 400 × 400 µm^2. For depth-profiling XPS and TOF-SIMS measurements of Li-metal anode, the Li-metal electrodes were obtained by disassembling the Li/HSE/Li symmetrical cells cycled with HSE-LiI or HSE (13:1) electrolytes at 0.1 mA cm^{-1} for 20 cycles (0.1 mAh cm^{-1}, 40 °C).

Batteries Assembly and Electrochemical Measurements: The ionic conductivity of the HSEs was calculated based on electrochemical impedance spectroscopy (EIS) data. The measurements were conducted from 10 MHz to 1 kHz with a sinusoidal signal (V_{rms} = 10 mV). The HSEs were sandwiched between two stainless steels (SS) in coin cells (with a surface area of 1.13 cm^2), and each test temperature was maintained for more than 30 min to ensure thermal equilibrium. The same protocol was also used for the EIS measurements of the Li//Li symmetric cells. The EIS data was fitted using an Equivalent Circuit (EC) model that included R_S as the series resistance, R_b as the bulk HSE resistance, and CPE_b as a Constant Phase Element (CPE) representing the bulk capacitance of the HSE membranes. Additionally, CPE_{int} was introduced to account for the capacitance associated with the blocking electrodes at low frequencies. Subsequently, the bulk resistance (R_b) and ionic conductivity (σ) were determined using the formula: $\sigma = d/(R_b \times A)$, with d representing the thickness of the HSE and A denoting the area of the HSE in contact with the stainless steels. The Li-ion transference numbers (t_{Li+}) of the HSEs were obtained from the symmetric Li//Li cell at 60 °C based on the equation: $t_{Li+} = I_s(V{-}I_0R_0)/I_0(V{-}I_sR_s)$, where V is the polarization voltage (10 mV), I_0 and R_0 are the current and resistance of the initial state and I_s and R_s are the current and resistance of the stable state. Linear-sweep voltammetry (LSV) curves were measured at a scan rate of 0.1 mV s^{-1} using Li/HSE/SS cells. All the EIS, t_{Li+}, and LSV data were collected from an Autolab PGSTAT302N workstation.

The galvanostatic charge-discharge tests of the Li//Li symmetric cell were performed on a Maccor 4000 battery cycler at 40 °C. The S@CNTs cathode mixture was made by first grinding sulfur powder and carbon nanotubes (CNTs) in a mortar with a mass ratio of 2:8, then transferring the mixture to a quartz ampule and heated to 155 °C for 6 h in an argon atmosphere. The cathode slurry was prepared by mixing S@CNTs, PEO, LiTFSI, and Super P with a mass ratio of 8: 0.5: 0.5: 1 in acetonitrile. Then, the slurry was spread evenly on aluminum foil to create a cathode film with loadings of ≈0.6 mg cm^{-2}, and dried under vacuum at 60 °C for 48 h. The all-solid-state Li/HSE/S@CNTs coin cells were assembled in a glove box filled with argon. Galvanostatic cycling was performed on a Maccor 4000 battery cycler at 60 °C.

Solid-State NMR Measurements: Solid-state NMR measurements were performed on a Bruker Ascend 500 MHz magnet (B0 = 11.7 T) equipped with a NEO console, operating at frequencies of 194.37 MHz for ^{7}Li, 73.6 MHz for ^{6}Li, 500.130 MHz for ^{1}H, and 125.758 MHz for ^{13}C. The chemical shifts of ^{6,7}Li were referenced with respect to a 0.1 м LiCl solution (0 ppm), while the ^{1}H and ^{13}C chemical shifts were referenced to solid adamantane (^{1}H at 1.81 ppm and ^{13}C at 38.48 ppm). A Bruker three-channel MAS 4 mm direct variable temperature (DVT) probe was used for all the measurements. Individual samples were prepared by cutting the HSEs membranes into small pieces, which were then transferred into 4 mm zirconia rotors and sealed with a Vespel cap. A MAS frequency of 10 kHz was applied for all the measurements.

One-pulse ^{7}Li and ^{6}Li experiments were performed with $\pi/2$ pulse lengths of 3.3 and 9 µs. A recycle delay of ≈4 times T_1 (spin-lattice relaxation time) was used for each nuclei, where the T_1 was determined using saturation recovery experiments. Variable temperature (VT) 2D ^{6}Li-^{6}Li EXSY measurements were performed for the HSE-LiI and HSE (13:1) samples at different mixing times. All 2D spectra consisted of 8 scans for each of the 1950 transients, each transient incremented by 8.5 µs. For 1D ^{7}Li CP MAS (^{1}H → ^{7}Li) experiments, a radio frequency (r.f.) field strengths of 81 kHz and various contact times were applied, the r.f. field amplitude of

© 2025 The Author(s). Advanced Energy Materials published by Wiley-VCH GmbH

16146840, 0, Downloaded from https://advanced.onlinelibrary.wiley.com/doi/10.1002/aenm.202406003 by Technical University Delft, Wiley Online Library on [06/06/2025]. See the Terms and Conditions (https://onlinelibrary.wiley.com/terms-and-conditions) on Wiley Online Library for rules of use; OA articles are governed by the applicable Creative Commons License

^{1}H during CP experiments was ramped from 70 to 100% and 128 scans were acquired for each sample with a recycle delay of 6 s. The 1D ^{6}Li CP MAS (^{1}H → ^{6}Li) experiments were performed with a contact time of up to 8 ms, the r.f. field amplitude of ^{1}H during CP experiments was ramped from 70 to 100% and 10240 scans were acquired for each sample with a recycle delay of 6 s. 2D ^{1}H-^{6}Li HETCOR measurements were performed with a short CP contact time of 0.5 ms for HSE-LiI and HSE (13:1). For each of the 128 transients in the indirect ^{1}H dimension, 1024 scans were accumulated. A recycle delay of 5 s was applied after each scan.

One-pulse ^{13}C measurements were conducted with a $\pi/2$ pulse length of 6.2 µs and a recycle delay of 1 s. The 1D ^{13}C CP MAS (^{1}H → ^{13}C) experiments were measured with an initial ^{1}H $\pi/2$ pulse of 3.8 µs and various contact times. An r.f. field strength of 64 kHz was applied, and 2048 scans were acquired for each sample with a recycle delay of 2 s. The data were fitted and deconvoluted using MestReNova 11. 2D ^{1}H-^{13}C HETCOR measurements were measured with a contact time of 2 ms for both HSE-LiI and HSE (13:1). For each of the 128 transients in the indirect ^{1}H dimension, 256 ^{13}C scans were accumulated. A recycle delay of 2 s was applied after each scan. For both the CP MAS and HETCOR experiments, proton decoupling was performed during acquisition using the SPINAL-64 decoupling sequence.

Pulsed-field gradient NMR (PFG-NMR) was used to determine the diffusion coefficients of ^{7}Li and ^{19}F for all the HSEs at VT (from 25 to 80 °C) using a Bruker Avance NEO 600 MHz narrow bore NMR spectrometer equipped with a diffusion probe. A stimulated echo sequence was used for all diffusion measurements. The typical diffusion time for both nuclei was 20 to 200 ms, gradient pulse duration was 2 ms. The maximum field strength was 7.05 T on a log scale. The diffusion coefficients were obtained by fitting the pulse data obtained with the Stejskal-Tanner Equation.[82]

Supporting Information

Supporting Information is available from the Wiley Online Library or from the author.

Acknowledgements

Financial support was greatly acknowledged by The Netherlands Organization for Scientific Research (NWO) under VICI grant 16122. Part of this work was also supported by the National Natural Science Foundation of China (No. 22479087 and 52203298), Guangdong Province Foundation for Distinguished Young Scholars (No. 2024B1515020092). S.Z. acknowledges the financial support from the China Scholarship Council. The authors thank Frans Ooms and Bart Boshuizen for assistance with the experiments.

Conflict of Interest

The authors declare no conflict of interest.

Author Contributions

S.Z., S.G., and M.W. planned the project. S.G. and M.W. supervised the project. S.Z. and S.G. carried out the NMR measurements. S.Z. prepared the samples and performed the electrochemistry, SEM, and XRD measurements. S.Z. and L.B. performed the XPS experiments. Y.L. performed the Raman, FT-IR, and TOF-SIMS measurements. S.G. assisted in NMR data analysis. L.B. assisted in XPS data analysis. M.L., S.G., L.B., and M.W. participated in discussing the results and commenting on the manuscript. The manuscript was mainly written and revised by S.Z., M.W., and S.G. All authors approved and revised the final version of the manuscript.

Data Availability Statement

The data that support the findings of this study are available from the corresponding author upon reasonable request.

Keywords

hybrid solid electrolytes, interface structure, ion conduction mechanism, solid-state NMR, structure-ion dynamics relationship

Received: December 19, 2024
Revised: February 21, 2025
Published online:

---

[1] Q. Zhao, S. Stalin, C.-Z. Zhao, L. A. Archer, *Nat. Rev. Mater.* **2020**, *5*, 229.
[2] J. Janek, W. G. Zeier, *Nat. Energy* **2016**, *1*, 16141.
[3] A. Manthiram, X. Yu, S. Wang, *Nat. Rev. Mater.* **2017**, *2*, 16103.
[4] X.-B. Cheng, C.-Z. Zhao, Y.-X. Yao, H. Liu, Q. Zhang, *Chem* **2019**, *5*, 74.
[5] T. Famprikis, P. Canepa, J. A. Dawson, M. S. Islam, C. Masquelier, *Nat. Mater.* **2019**, *18*, 1278.
[6] A. Banerjee, X. Wang, C. Fang, E. A. Wu, Y. S. Meng, *Chem. Rev.* **2020**, *120*, 6878.
[7] Z. Gao, H. Sun, L. Fu, F. Ye, Y. Zhang, W. Luo, Y. Huang, *Adv. Mater.* **2018**, *30*, 1705702.
[8] X. Lu, Y. Wang, X. Xu, B. Yan, T. Wu, L. Lu, *Adv. Energy Mater.* **2023**, *13*, 2301746.
[9] D. Zhang, X. Meng, W. Hou, W. Hu, J. Mo, T. Yang, W. Zhang, Q. Fan, L. Liu, B. Jiang, L. Chu, M. Li, *Nano Res. Energy* **2023**, *2*, 9120050.
[10] Z. Zhang, X. Wang, X. Li, J. Zhao, G. Liu, W. Yu, X. Dong, J. Wang, *Mater. Today Sustain.* **2023**, *21*, 100316.
[11] T. T. Vu, H. J. Cheon, S. Y. Shin, G. Jeong, E. Wi, M. Chang, *Energy Storage Mater.* **2023**, *61*, 102876.
[12] A.-G. Nguyen, C.-J. Park, *J. Membr. Sci.* **2023**, *675*, 121552.
[13] Z. Xue, D. He, X. Xie, *J. Mater. Chem. A.* **2015**, *3*, 19218.
[14] J. Feng, L. Wang, Y. Chen, P. Wang, H. Zhang, X. He, *Nano Converg.* **2021**, *8*, 2.
[15] H. Huo, Y. Chen, J. Luo, X. Yang, X. Guo, X. Sun, *Adv. Energy Mater.* **2019**, *9*, 1804004.
[16] M. Zhang, A. Yusuf, D.-Y. Wang, *J. Power Sources* **2024**, *591*, 233812.
[17] S. Xue, S. Chen, Y. Fu, H. Zhu, Y. Ji, Y. Song, F. Pan, L. Yang, *Small* **2023**, *19*, 2305326.
[18] Y. Fu, K. Yang, S. Xue, W. Li, S. Chen, Y. Song, Z. Song, W. Zhao, Y. Zhao, F. Pan, L. Yang, X. Sun, *Adv. Funct. Mater.* **2023**, *33*, 2210845.
[19] X. Zhang, C. Fu, S. Cheng, C. Zhang, L. Zhang, M. Jiang, J. Wang, Y. Ma, P. Zuo, C. Du, Y. Gao, G. Yin, H. Huo, *Energy Storage Mater.* **2023**, *56*, 121.
[20] J. Zheng, Y.-Y. Hu, *ACS Appl. Mater. Interfaces* **2018**, *10*, 4113.
[21] H.-R. Wang, Y.-N. Yang, T. Zhang, *ACS Appl. Energy Mater.* **2023**, *6*, 2031.
[22] W. Liu, F. Deng, S. Song, G. Ji, N. Hu, C. Xu, *Mater. Technol.* **2020**, *35*, 618.
[23] G. Yang, Y. Song, Q. Wang, L. Zhang, L. Deng, *Mater. Des.* **2020**, *190*, 108563.
[24] S. Xiao, L. Ren, W. Liu, L. Zhang, Q. Wang, *Energy Storage Mater.* **2023**, *63*, 102970.
[25] P. Hu, J. Chai, Y. Duan, Z. Liu, G. Cui, L. Chen, *J. Mater. Chem. A.* **2016**, *4*, 10070.
[26] Z. Li, J. Fu, X. Zhou, S. Gui, L. Wei, H. Yang, H. Li, X. Guo, *Adv. Sci.* **2023**, *10*, 2201718.
[27] F. Zhu, S. Ho-Sum Cheng, Y. Xu, W. Liao, K. He, D. Chen, C. Liao, X. Cheng, J. Tang, R. K. Y. Li, C. Liu, *Compos. Sci. Technol.* **2021**, *210*, 108837.
[28] K. Fan, X. Lai, Z. Zhang, L. Chai, Q. Yang, G. He, S. Liu, L. Sun, Y. Zhao, Z. Hu, L. Wang, *J. Power Sources* **2023**, *580*, 233342.

© 2025 The Author(s). Advanced Energy Materials published by Wiley-VCH GmbH

16146840, 0, Downloaded from https://advanced.onlinelibrary.wiley.com/doi/10.1002/aenm.202406003 by Technical University Delft, Wiley Online Library on [06/06/2025]. See the Terms and Conditions (https://onlinelibrary.wiley.com/terms-and-conditions) on Wiley Online Library for rules of use; OA articles are governed by the applicable Creative Commons License

[29] X. Yang, J. Liu, N. Pei, Z. Chen, R. Li, L. Fu, P. Zhang, J. Zhao, *Nano-Micro Lett.* **2023**, *15*, 74.
[30] X. Su, X.-P. Xu, Z.-Q. Ji, J. Wu, F. Ma, L.-Z. Fan, *Electrochem. Energy Rev.* **2024**, *7*, 2.
[31] H. Su, Y. Zhong, C. Wang, Y. Liu, Y. Hu, J. Li, M. Wang, L. Jiao, N. Zhou, B. Xiao, X. Wang, X. Sun, J. Tu, *Nat. Commun.* **2024**, *15*, 2552.
[32] M. Takahashi, T. Watanabe, K. Yamamoto, K. Ohara, A. Sakuda, T. Kimura, S. Yang, K. Nakanishi, T. Uchiyama, M. Kimura, A. Hayashi, M. Tatsumisago, Y. Uchimoto, *Chem. Mater.* **2021**, *33*, 4907.
[33] S.-J. Choi, S.-H. Choi, A. D. Bui, Y.-J. Lee, S.-M. Lee, H.-C. Shin, Y.-C. Ha, *ACS Appl. Mater. Interfaces* **2018**, *10*, 31404.
[34] M. Liu, S. Zhang, R. van Eck, C. Wang, S. Ganapathy, M. Wagemaker, *Nat. Nanotechnol.* **2022**, *55*, 959.
[35] P. Ranque, J. Zagórski, S. Devaraj, F. Aguesse, J. M. López del Amo, *J. Mater. Chem. A.* **2021**, *9*, 17812.
[36] J. Zheng, H. Dang, X. Feng, P.-H. Chien, Y.-Y. Hu, *J. Mater. Chem. A.* **2017**, *5*, 18457.
[37] J. Zheng, M. Tang, Y.-Y. Hu, *Angew. Chem., Int. Ed.* **2016**, *55*, 12538.
[38] M. Wagemaker, A. P. M. Kentgens, F. M. Mulder, *Nature* **2002**, *418*, 397.
[39] S. Ganapathy, E. R. H. van Eck, A. P. M. Kentgens, F. M. Mulder, M. Wagemaker, *Chem. – Eur. J.* **2011**, *17*, 14811.
[40] H. Wang, T. Hou, H. Cheng, B. Jiang, H. Xu, Y. Huang, *J. Energy Chem.* **2022**, *71*, 218.
[41] Q. Han, S. Wang, L. Wang, W. Ren, F. Zhang, J. Lu, H. Wang, *Adv. Energy Mater.* **2023**, *13*, 2301462.
[42] M. Liu, C. Wang, C. Zhao, E. van der Maas, K. Lin, V. A. Arszelewska, B. Li, S. Ganapathy, M. Wagemaker, *Nat. Commun.* **2021**, *12*, 5943.
[43] X. Ao, X. Wang, J. Tan, S. Zhang, C. Su, L. Dong, M. Tang, Z. Wang, B. Tian, H. Wang, *Nano Energy* **2021**, *79*, 105475.
[44] D. G. Mackanic, W. Michaels, M. Lee, D. Feng, J. Lopez, J. Qin, Y. Cui, Z. Bao, *Adv. Energy Mater.* **2018**, *8*, 1800703.
[45] I. Hanghofer, M. Brinek, S. L. Eisbacher, B. Bitschnau, M. Volck, V. Hennige, I. Hanzu, D. Rettenwander, H. M. R. Wilkening, *Phys. Chem. Chem. Phys.* **2019**, *21*, 8489.
[46] B. Chen, T. Wang, C. Liu, T. Li, X. Liu, *Angew. Chem., Int. Ed.* **2024**, *63*, 202400960.
[47] J. Xu, J. Li, Y. Li, M. Yang, L. Chen, H. Li, F. Wu, *Adv. Mater.* **2022**, *34*, 2203281.
[48] Y. Yusim, E. Trevisanello, R. Ruess, F. H. Richter, A. Mayer, D. Bresser, S. Passerini, J. Janek, A. Henss, *Angew. Chem., Int. Ed.* **2023**, *62*, 2218316.
[49] F. J. Simon, M. Hanauer, F. H. Richter, J. Janek, *ACS Appl. Mater. Interfaces* **2020**, *12*, 11713.
[50] H. Huo, M. Jiang, B. Mogwitz, J. Sann, Y. Yusim, T.-T. Zuo, Y. Moryson, P. Minnmann, F. H. Richter, C. Veer Singh, J. Janek, *Angew. Chem., Int. Ed* **2023**, *62*, 202218044.
[51] F. J. Simon, M. Hanauer, A. Henss, F. H. Richter, J. Janek, *ACS Appl. Mater. Interfaces* **2019**, *11*, 42186.
[52] S. Xu, Z. Sun, C. Sun, F. Li, K. Chen, Z. Zhang, G. Hou, H.-M. Cheng, F. Li, *Adv. Funct. Mater.* **2020**, *30*, 2007172.
[53] T. Koster, L. Vanwullen, *Solid State Ion.* **2008**, *178*, 1879.
[54] J. R. Wickham, R. N. Mason, C. V. Rice, *Solid State Nucl. Magn. Reson.* **2007**, *31*, 184.
[55] N. Boaretto, P. Ghorbanzade, H. Perez-Furundarena, L. Meabe, J. M. López del Amo, I. E. Gunathilaka, M. Forsyth, J. Schuhmacher, A. Roters, S. Krachkovskiy, A. Guerfi, M. Armand, M. Martinez-Ibañez, *Small* **2023**, *34*, 2305769.
[56] H. Huo, M. Jiang, B. Mogwitz, J. Sann, Y. Yusim, T.-T. Zuo, Y. Moryson, P. Minnmann, F. H. Richter, C. Veer Singh, J. Janek, *Angew. Chem., Int. Ed.* **2023**, *62*, 202218044.
[57] T. K. Schwietert, V. A. Arszelewska, C. Wang, C. Yu, A. Vasileiadis, N. J. J. de Klerk, J. Hageman, T. Hupfer, I. Kerkamm, Y. Xu, E. van der Maas, E. M. Kelder, S. Ganapathy, M. Wagemaker, *Nat. Mater.* **2020**, *19*, 428.
[58] D. S Jolly, D. L. R. Melvin, I. D. R. Stephens, R. H. Brugge, S. D. Pu, J. Bu, Z. Ning, G. O. Hartley, P. Adamson, P. S. Grant, A. Aguadero, P. G. Bruce, *Inorganics* **2022**, *10*, 60.
[59] S. Lascaud, M. Perrier, A. Vallee, S. Besner, J. Prud'homme, M. Armand, *Macromolecules* **1994**, *27*, 7469.
[60] W. Wieczorek, D. Raducha, A. Zalewska, J. R. Stevens, *J. Phys. Chem. B.* **1998**, *102*, 8725.
[61] R. Fang, B. Xu, N. S. Grundish, Y. Xia, Y. Li, C. Lu, Y. Liu, N. Wu, J. B. Goodenough, *Angew. Chem.* **2021**, *133*, 17842.
[62] K. Kulasekarapandian, S. Jayanthi, A. Muthukumari, A. Arulsankar, B. Sundaresan, *Int. J. Eng. Res. Dev.* **2013**, *5*, 30.
[63] T. H. Hester, D. E. Castillo, D. J. Goebbert, *Rapid Commun. Mass Spectrom.* **2013**, *27*, 1643.
[64] M. Zhao, B.-Q. Li, X.-Q. Zhang, J.-Q. Huang, Q. Zhang, *ACS Cent. Sci.* **2020**, *6*, 1095.
[65] F. Wu, J. T. Lee, N. Nitta, H. Kim, O. Borodin, G. Yushin, *Adv. Mater.* **2014**, *27*, 101.
[66] S. Kim, Y. M. Kwon, K. Y. Cho, S. Yoon, *Electrochim. Acta.* **2021**, *391*, 138927.
[67] G. Wang, X. Xiong, D. Xie, X. Fu, X. Ma, Y. Li, Y. Liu, Z. Lin, C. Yang, M. Liu, *Energy Storage Mater.* **2019**, *23*, 701.
[68] F. Han, J. Yue, X. Zhu, C. Wang, *Adv. Energy Mater.* **2018**, *8*, 1703644.
[69] Z. Wu, R. Wang, C. Yu, C. Wei, S. Chen, C. Liao, S. Cheng, J. Xie, *Ind. Eng. Chem. Res.* **2022**, *62*, 96.
[70] X. Han, J. Cai, X. Wang, Y. Liu, H. Zhou, X. Meng, *Mater. Today Commun.* **2021**, *26*, 101934.
[71] E. Peled, I. Shekhtman, T. Mukra, M. Goor, I. Belenkaya, D. Golodnitsky, *J. Electrochem. Soc.* **2017**, *165*, A6051.
[72] C. Xu, B. Sun, T. Gustafsson, K. Edström, D. Brandell, M. Hahlin, *J. Mater. Chem. A* **2014**, *2*, 7256.
[73] J. Zhang, S. Li, X. Wang, S. Mao, J. Guo, Z. Shen, J. Mao, Q. Wu, K. Shen, H. Cheng, Y. Tan, Y. Lu, *Adv. Energy Mater.* **2023**, *13*, 2302587.
[74] F. Walther, R. Koerver, T. Fuchs, S. Ohno, J. Sann, M. Rohnke, W. G. Zeier, J. Janek, *Chem. Mater.* **2019**, *31*, 3745.
[75] O. Sheng, H. Hu, T. Liu, Z. Ju, G. Lu, Y. Liu, J. Nai, Y. Wang, W. Zhang, X. Tao, *Adv. Funct. Mater.* **2022**, *32*, 2111026.
[76] M. Li, H. An, Y. Song, Q. Liu, J. Wang, H. Huo, S. Lou, J. Wang, *J. Am. Chem. Soc.* **2023**, *145*, 25632.
[77] C. Gong, S. D. Pu, X. Gao, S. Yang, J. Liu, Z. Ning, G. J. Rees, I. Capone, L. Pi, B. Liu, G. O. Hartley, J. Fawdon, J. Luo, M. Pasta, C. R. M. Grovenor, P. G. Bruce, A. W. Robertson, *Adv. Energy Mater.* **2021**, *11*, 2003118.
[78] R. Guo, B. M. Gallant, *Chem. Mater.* **2020**, *32*, 5525.
[79] M. S. Kim, Z. Zhang, P. E. Rudnicki, Z. Yu, J. Wang, H. Wang, S. T. Oyakhire, Y. Chen, S. C. Kim, W. Zhang, D. T. Boyle, X. Kong, R. Xu, Z. Huang, W. Huang, S. F. Bent, L.-W. Wang, J. Qin, Z. Bao, Y. Cui, *Nat. Mater.* **2022**, *21*, 445.
[80] M. S. Kim, Z. Zhang, J. Wang, S. T. Oyakhire, S. C. Kim, Z. Yu, Y. Chen, D. T. Boyle, Y. Ye, Z. Huang, W. Zhang, R. Xu, P. Sayavong, S. F. Bent, J. Qin, Z. Bao, Y. Cui, *ACS Nano* **2023**, *17*, 3168.
[81] S. Liu, X. Ji, N. Piao, J. Chen, N. Eidson, J. Xu, P. Wang, L. Chen, J. Zhang, T. Deng, S. Hou, T. Jin, H. Wan, J. Li, J. Tu, C. Wang, *Angew. Chem., Int. Ed.* **2021**, *60*, 3661.
[82] E. O. Stejskal, J. E. Tanner, *J. Chem. Phys.* **1965**, *42*, 288.

© 2025 The Author(s). Advanced Energy Materials published by Wiley-VCH GmbH

16146840, 0, Downloaded from https://advanced.onlinelibrary.wiley.com/doi/10.1002/aenm.202406003 by Technical University Delft, Wiley Online Library on [06/06/2025]. See the Terms and Conditions (https://onlinelibrary.wiley.com/terms-and-conditions) on Wiley Online Library for rules of use; OA articles are governed by the applicable Creative Commons License